Journal of Power Sources 436 (2019) 226838

Contents lists available at ScienceDirect

Journal of Power Sources

journal homepage: www.elsevier.com/locate/jpowsour

Model-assisted identification of solid oxide cell elementary processes by electrochemical impedance spectroscopy measurements

P. Caliandro [a,*], A. Nakajo [a,b], S. Diethelm [a,b], J. Van herle [a]

[a] Group of Energy Materials (GEM), École Polytechnique Fédérale de Lausanne, 1951, Sion, Switzerland
[b] SOLIDpower SA, 1400, Yverdon-les-Bains, Switzerland

HIGHLIGHTS

- Operating conditions influence on DRT signals of experimentally recorded data.
- Attribution of peaks-to-processes clarified in the middle frequency range: 10–500 Hz.
- Peaks-to-processes attribution supported by the DRT of numerically modeled spectra.
- Influence of test cell geometry and frequency range on the deconvoluted spectra.

ARTICLE INFO

Keywords:
Electrochemical impedance spectroscopy (EIS)
Distribution of relaxation time constants (DRT)
Solid oxide cell (SOC)
Dynamic physically-based model
Sensitivity analysis

ABSTRACT

Electrochemical Impedance Spectroscopy (EIS) is extensively used to characterize Solid Oxide Cells (SOCs) to extract information on the elementary loss mechanisms. However, these individual mechanisms usually overlap in the frequency domain, requiring dedicated data processing for unambiguous identification. A powerful method for discriminating process contributions is the analysis by the Distribution of Relaxation Times (DRT). The de-convoluted spectrum of SOC generally presents, six peaks from mHz to hundreds of kHz. DRT peak-to-process attribution is often obtained by experimental sensitivity analysis. In the study, six parameters have been systematically varied: temperature, current density, partial pressure of O2 at the oxygen electrode, partial pressure of steam at the fuel electrode, total flow rates and fuel composition. The effect of wires inductance and different cell geometries has also been analyzed. The study provides detailed information about the contribution of the elementary processes to the total losses over a wide range of operation regimes. It further refines peak-to-process attributions by using a dynamic numerical model that includes gas and solid phase transport coupled with charge transfer and chemical reactions. Moreover, the non-univocal literature attribution of processes in the middle frequency range is clarified: strongly overlapping peaks cannot be separated even by DRT.

1. Introduction

Solid Oxide cells are highly efficient electrochemical devices able to directly transform fuel into electricity (fuel cell mode) and vice versa (electrolyzer mode).

The high operating temperature provides fuel flexibility, allowing the use of gas, such as methane, syngas, ammonia. Methane in particular is of interest because the use of the existing network can help a softer energy transition. In parallel, the interest in electrolysers is ever increasing for the storage of the excess energy produced by renewables.

Despite the significant technological advantages, the wide scale commercialization of the SOC technology is slowed down by remaining costs and lifetime limitations.

Electrochemical Impedance Spectroscopy (EIS) is a powerful non-destructive characterization technique. It is relevant for improving the durability of SOC devices, by identifying the effect of degradation phenomena taking place in a stack under operation. The technique consists in measuring the system response upon the application of a periodic stimulus perturbation (voltage or current) over a specified range of frequencies. Since phenomena such as gas-phase transport from/to electroactive sites, solid state oxygen vacancy diffusion and charge transfer, have different dynamics, they manifest themselves at different frequencies, which potentially allows their discrimination.

Since these time constants are highly overlapped, the measurement

* Corresponding author.
E-mail address: priscilla.caliandro@epfl.ch (P. Caliandro).

https://doi.org/10.1016/j.jpowsour.2019.226838
Received 2 May 2019; Received in revised form 23 June 2019; Accepted 1 July 2019
Available online 31 July 2019

Table 1
DRT peaks to processes attribution of anode supported SOFC obtained by different authors under different operating conditions.

Freq. (Hz)	0.1–1	1–10	10–100	100–1000	10^3–10^4	10^4–10^5
[1] **KIT**	FE diff. (support)	–	OE	FE diff. (AFL)	FE ct	High f peak
Freq. (Hz)	0.1–1	1–10	10–50	50–100	500–10^3	10^3–10^4
[2] **DTU**	–	conv.	FE diff.	OE	FE diff.+ ct	
[3] **HTc**	OE diff	conv.	OE or FE diff.	OE or FE diff.	FE c.t.	SS interf.

OE: oxygen electrode **AFL:** anode functional layer **FE:** fuel electrode **conv.:** conversion **diff.:** diffusion **ct:** charge transfer **SS interf.:** solid-solid interface.

data needs to be processed with the distribution of relaxation time constants (DRT) methodology that allows for the breakdown of losses by performing a deconvolution of the electrochemical impedance (EI) spectrum. It is however important to remember that DRT is a comparative method; thus, in order to attribute peaks to phenomena and gain useful information about the loss contributions, a meaningful comparison has to be carried out. A sensitivity analysis is generally required. Systematic variations of the operating parameters (temperature, current, gas composition, etc.) can allow identifying which processes are affected. For example, changing the temperature can inform about thermally activated processes, whereas changing the flows or gas composition will give insights on concentration and diffusion losses. DRT analysis conducted by three different authors [1–3] is presented in Table 1. From Table 1 it is clear that peak identification is not univocal. In general, five to six peaks are distinguished, which can shift in frequency and describe different processes if the SOCs are tested in different conditions. Moreover, the overlapping of physical phenomena in the same frequency range adds complexity to the non-trivial situation. The usual frequency range in measured EIS spans from 0.1 to 10^5 Hz. This interval can be divided into 4 decades plus two extreme intervals at low and high frequency. According to different references [1–6] a summary of the possible peaks attribution is reported as follows:

- P1 - f < 1 Hz: fuel electrode diffusion under reformed gas operation and/or oxygen electrode adsorption/desorption;
- P2 - f = 1–10 Hz: gas conversion;
- P3 - f = 10–100 Hz: overlap of oxygen and transport related processes in the fuel electrode;
- P4 - f = 100–1000 Hz: overlap of oxygen and transport related processes in the fuel electrode;
- P5 - f = 1–10 kHz: attribution to charge transfer in the fuel electrode;
- P6 - f > 10 kHz: only observed for measurement conducted at high frequency, and no consensus exists in literature.

A unique attribution is not possible due to the sensitivity of the peaks to differences in experimental setup geometry, microstructural parameters, and operating conditions. Yet shedding more light on peak attribution is necessary and is expected achievable. In this paper, an experimental sensitivity analysis is coupled to a numerical model to improve peak attribution capabilities.

2. EIS model

Attributing processes to peaks is particularly difficult in the middle frequency range where both fuel and oxygen electrode phenomena overlap. In order to understand better the expected spectral position and characteristics of peaks related to transport (solid and gas phase), a numerical model of the complete cell was used.

2.1. Numerical model

The numerical model is adapted from Ref. [7] to study the contribution of transport limitations on the impedance spectra. The original model [7] is a one-dimensional electrochemical model which includes gas convection (along y-axis) and solid phase transport coupled with charge transfer and chemical reactions in the porous electrodes (along z-axis). The equation's solutions along the y-axis are the boundary conditions for the governing equations solved along the z-axis. The modifications for this study are as follows:

(i) An isothermal model is considered as a first approximation, which allows discarding the energy conservation equations.
(ii) Transient terms are added to the species conservation equations along the two gas channels (y direction) considering co-flow configuration between air-fuel:

$$\frac{\partial c_{Mi}}{\partial t}+\frac{\partial\left(\rho_g v_g x_i\right)}{\partial y}=\frac{1}{\delta_g}M_i n_i \tag{1}$$

where c_{Mi} is the mass concentration of the species, and ρ_g v_g are the density and velocity of the gas mixture, x_i is the molar fraction of species, n_i is the molar flux of species, M_i is the molar mass and δ_g is the height of the gas channel.

(iii) The electrochemical processes are modeled with global Butler-Volmer kinetics with apparent concentration dependencies (Eq. (2)) [8].

$$i=i_0^*\frac{\left(\frac{x_{H_2}^{TPB}}{x_{H_2}^*}\right)^{(1-\alpha_a/2)}\left(x_{H_2O}^{TPB}\right)^{\alpha_a/2}}{1+\left(\frac{x_{H_2}^{TPB}}{x_{H_2}^*}\right)^{(1/2)}}\left[\exp\left(\frac{\alpha_a F\eta_{act,a}}{RT}\right)-\exp\left(\frac{-\alpha_c F\eta_{act,a}}{RT}\right)\right] \tag{2}$$

Here $x_{H_2}^*$ depends upon hydrogen desorption/adsorption and it is calculated according to an Arrhenius type equation [7,8], $x_{H_2}^{TPB}$ and $x_{H_2O}^{TPB}$ are the species at the electrode-electrolyte interface resulting from the DGM (Dusty Gas model). The charge transfer coefficients (α_a, α_c) for the hydrogen and reforming mixture have been directly estimated from experimental data. This expression is used to simulate the correct source/sink term for the species profile at the TPBs within the electrode. Since capacity effects are not considered, no charge transfer peak will appear in the DRT plot of the simulated spectra. Expression (Eq. (2)) has been modified for the CO/CO_2 mixture following the approach reported in Ref. [9]. The constants have been corrected to obtain the same anodic overpotential difference between 50 and 50%CO/CO_2 and H_2/H_2O mixture as reported in Ref. [10].

(iv) The transient Dusty Gas model governing equations are solved considering diffusion and reaction in the fuel electrode support. The only different term with respect to the original formulation is reported in Eq. (3).

$$\varepsilon\frac{\partial c_i}{\partial t}+\frac{\partial n_i}{\partial z}=\Re_i \tag{3}$$

The equation is solved in the fuel electrode thickness (z). Here $\Re_i$ is the rate of production of species i given by the chemical reaction occurring in the support.

(v) The same is done on the oxygen electrode side (Eq. (4)).

$$\varepsilon\frac{\partial c_{O_2}}{\partial t}+\frac{\partial n_{O_2}}{\partial z}=\frac{a_{MIEC}\Re_{MIEC}}{2} \tag{4}$$

where a_{MIEC} is the volume specific interfacial surface area between pore and the MIEC (mixed ionic electronic conductor) material and $\Re_{MIEC}$ is the surface reaction rate. The single solid-phase MIEC formulation has

been used to model the oxygen electrode, which is composed of three layers. The first is a LSCF:GDC composite where the effective material properties are estimated by weighting those of the two phases. The second layer is constituted only by LSCF, and in the third (the contact layer), only gas phase transport is simulated and no vacancy transport or reactions occur. The transient term has been added in the cathode vacancy conservation equation (Eq. (5)):

$$(1-\varepsilon)\frac{\partial c_v}{\partial t} + D_v\frac{\partial^2 c_v}{\partial z^2} = a_{MIEC}\Re_{MIEC} \tag{5}$$

(vi) The total cell voltage is:

$$U = E^0 + \frac{RT}{2F}\ln\left(\frac{p_{H_2}^{TPB}\left(p_{O_2}^{TPB}\right)^{0.5}}{p_{H_2O}^{TPB}}\right) - R_{ohm}i - \eta_{fl} - \eta_{ox} \tag{6}$$

with $\eta_{ox} = -\frac{RT}{2F}\ln\frac{c_v|_{MIEC-e}}{c_v^o}$ where p_x^{TPB} are the species partial pressure at the electrode-electrolyte interface resulting from DGM, η_{fl} results from Eq. (2) and c_v^o is the equilibrium vacancy concentration.

Dedicated fitting of the model on single cell experiments has not been performed. Simulations were performed using parameters estimated previously [7], because the objective is to support the processing of the experimental observation based upon the analysis of trends and regimes.

The resolution of the transient model governing equations needs initial conditions, which are provided by the solution of the steady state problem. An alternating total current density is imposed to simulate the transient behavior. The total current density is defined as the integral over the radius of a single cell or the length of the stack channel of the local current density which has a spatial distribution; in the isothermal conditions of the present study, it decreases by moving from the inlet towards the outlet. To simulate an impedance spectrum, the sinusoidal current has to be simulated at different frequencies (Eq. (7)) each time over a variable period of time.

$$i = i_{bias} + i_{ampl}\sin(2\pi f \times t) \tag{7}$$

Direct sweeping from low to high frequency, practically compromised solver convergence. A dimensionless approach was applied to overcome this difficulty. The frequency of the imposed current perturbation is always the same and applied for a fixed period (20 s). The actual modification of frequency was instead achieved by the scaling of to the transient terms in the governing equations (example in Eq. (8)). Therefore, each discrete simulated frequency requires a distinct model run, which was implemented in an automated manner. In this way, stable solver operation and rapid convergence was systematically achieved over the whole investigated range of frequencies.

$$f\frac{\partial c_{Mi}}{\partial t} + \frac{\partial\left(\rho_g v_g x_i\right)}{\partial y} = \frac{1}{\delta_g}M_i n_i \tag{8}$$

Computing the impedance corresponds to calculating the ratio between the module of the imposed current and the obtained voltage and the phase shift between the two signals:

$$Z(\omega) = \frac{|U(\omega)|}{|I(\omega)|}e^{j\vartheta(\omega)} \tag{9}$$

where the phase shift ϑ is computed using the Matlab script PhDiff [11].

3. Experiment

Single cells are characterized and operated in a radial metallic test rig (Crofer 22 APU) [12]. It is constituted by two flanges that allow for: providing the gases at the fuel and air side, and imposing constant mechanical compression force through springs. The flanges are square plates and can accommodate a disk cell up to 60 mm in diameter. Gold meshes are used for current collection on the air electrode. Ni foam 0.5 mm thick is used as current collector for the fuel electrode. The two atmosphere compartments are separated by a glass sealing applied at the periphery of the cell by a dispenser. As suggested in Ref. [13], current and voltage wire pairs need to be twisted to minimize the mutual inductance effect, while measuring impedance spectra. The original configuration of the wires was accordingly modified. IV curves and EI spectra are recorded with Zahner ZENNIUM Electrochemical Workstations. For currents higher than 2.5 A, an external potentiostat (PP201) able to reach 20 A is used. The experiments presented in this work are performed on SOC ASC from SOLIDpower.

SOLIDpower cells are standard Ni-YSZ anode-supported cells, on which an electrolyte (YSZ), a barrier layer (GDC), LSCF:GDC composite cathode, LSCF, and current collector layer are deposited and sintered. The cells are produced by anode and electrolyte co-casting and co-sintering followed by screen-printing of the cathode layers. The cell layers' thicknesses are 240 μm for the anode support, 10 μm for the thin electrolyte, 6–8 μm for the barrier layer, and 60 μm for the bilayer cathode, respectively.

Table 2
Parameters used during measurements for the simulation of EIS spectra at different temperatures.

Parameter	Unit				
Total flows	NmL min^{-1}	Air		Fuel	
		200		200	
Composition	%	pO_2	pN_2	pH_2	pH_2O
		21%	79%	50%	50%
Bias current	A cm^{-2}	0.3			
Perturbation current	A	0.05			
Temperature	**°C**	**750**	**785**	**800**	**850**
OCV recorded	V	0.95	0.938	0.933	0.916
OCV theoretical	V	0.955	0.944	0.939	0.924
Difference	mV	5	6	6	8

Table 3
Parameters used during measurements for the simulation of EIS spectra at different current densities.

Parameter	Unit					
Total flow rates	NmL min^{-1}	Air		Fuel		
		400		200		
Composition	%	pO_2	pN_2	pH_2		pH_2O
		21	79	50		50
Bias current	**A cm^{-2}**	**−0.5**	**−0.25**	**0**	**0.25**	**0.5**
Perturbation current	A	0.05				
Temperature	°C	785				
OCV recorded	V	0.938				
OCV theoretical	V	0.944				
Difference	mV	6				

4. Results and discussion

Six operation parameters were systematically varied during the experiment on the same cell: temperature, current density, partial pressure of O_2 at the oxygen electrode, partial pressure of steam at the fuel electrode, fuel composition, and total gas flow rates (air and fuel). The cell is assembled as described before; twisted wires allow obtaining inductance free spectra in which the high frequency semicircle does not intersect the real axis even at 100 kHz. For higher frequency, an unusual behavior was observed and resulted in the transformation of inductive effects into capacitive ones. For this reason, the last five points of the spectra were discarded. Nevertheless, the spectra behavior at higher frequencies (>100 kHz) was extrapolated before deconvolution. Tests

Table 4
Parameters used during measurements for the simulation of EIS spectra at different oxygen partial pressure.

Parameter	Unit							
Total flow rates	NmL min^{-1}	Air				Fuel		
		200				200		
Composition	**%**	**pO_2**		pN_2		pH_2		pH_2O
		Variable		1-pO_2		50		50
		100	**50**	**21**	**15**	**10**	**7.5**	**5**
Bias current	A cm^{-2}	0.3						
Perturbation current	A	0.05						
Temperature	°C	800						
OCV recorded	V	0.97	0.954	0.933	0.925	0.915	0.907	0.897
OCV theoretical	V	0.975	0.96	0.939	0.932	0.922	0.916	0.906
Difference	mV	5	5.6	6.5	6.7	7	8.7	9

Table 5
Parameters used during measurements for the simulation of EIS spectra at different steam partial pressure.

Parameter	Unit							
Total flow rates	NmL min^{-1}	Air				Fuel		
		200				200		
Composition	**%**	pO_2		pN_2		pH_2		**pH_2O**
		21		79		1-pH_2O		**Variable**
		60	**55**	**50**	**40**	**30**	**20**	**10**	**5**
Bias current	A cm^{-2}	0						
Perturbation current	A	0.05						
Temperature	°C	800						
OCV recorded	V	0.915	0.927	0.933	0.953	0.972	0.996	1.035	1.068
OCV theoretical	V	0.92	0.93	0.939	0.958	0.978	1.003	1.04	1.076
Difference	mV	5	3	6	5	6	7	5	8

showed that the DRT spectra obtained with either the Fourier [14] and Tikhonov [15] techniques show good agreement, hence only results using the latter (Tikhonov) is reported here.

Tables 2–7 lists the working conditions at which the spectra were recorded. These values are also used as inputs for the numerical simulations. As specified before, the numerical model is not dynamic in terms of charge transfer, thus the associated high frequency peak does not appear in the simulated spectra. In the compiled figures, the measured spectra are reported on the left and simulated ones on the right. For each figure, the plot (e) and (f) represent the evolution of the resistances (areas integrated below each peak) and time constants ($\tau = 1/f$) extracted from the DRT plots of the measured spectra. In the (e) subplot of all the figures, the ohmic resistance (Rs) and the total polarization resistance (Rp), retrieved from the Nyquist plot, are reported. Moreover, the sum of the individual peak resistances (SUM) is compared with the polarization resistance obtained from the Nyquist plot (Rp). The consistency of all the spectra has been checked by the linear KK test [16,17].

Table 6
Parameters used during measurements for the simulation of EIS spectra at different fuel compositions.

Parameter	Unit					
Total flow rates	Nml min^{-1}	Air		Fuel		
		200		200	100	150
Composition	**%**	pO_2	pN_2	**pH_2-pH_2O**	**Int SMR**	**Ext SMR**
		21	79	**50–50**	*	**
Bias current	A cm^{-2}	0.3				
Perturbation current	A	0.05				
Temperature	°C	800				
OCV recorded	V			0.933	1.004	0.997
OCV theoretical	V			0.939	0.897	0.897
Difference	mV			6	107	100

* Internal SMR **pH_2O:50% - pCH_4: 25% - pN_2: 25%.**
** External SMR **pH_2:53.3% - pH_2O:13.3% - pCO:13.2% - pCO_2:3.5% - pCH_4:0% - pN_2:16.7%.**

4.1. Temperature

To investigate the DRT peaks dependence upon temperature variation four values of temperature have applied within a range from 750 °C to 850 °C. The fuel electrode is fed with a binary mixture of H_2/H_2O 50-50%, to minimize the conversion losses, while air is sent to the oxygen electrode (Table 2). The measured OCV values at the four temperatures are reported in Table 2. The difference between these values and the theoretical values, is around 6 mV. When dry H_2 (100% molar fraction) was measured, the OCV value was 1.23 V, indicating that the partial pressure of steam in the fuel compartment was as low as 0.18%. This small difference confirms that a good sealing was achieved during the assembly.

In Fig. 1(a), the Nyquist plot of the spectra at the four temperatures is reported. As expected, increasing the temperature causes a shift of the spectra to the left (smaller resistances), because of improved ionic conductivity of YSZ, GDC and LSCF as well as the electronic conductivity of LSCF. The DRT plot (Fig. 1(c)) highlights that the high frequency regime is more influenced by the temperature increase, whereas the low frequency region is almost insensitive. The peaks P5 and P6 experience the most significant reduction. The resistance associated to P5 drops

Table 7
Parameters used during measurements for the simulation of EIS spectra at different total flows.

Parameter	Unit				
Total flow rate	Nml min^{-1}	Air-Fuel			
		100–200	200–200	200–400	400–400
Composition	%	pO_2	pN_2	pH_2	pH_2O
		21%	79%	50%	50%
Bias current	A cm^{-2}	0.3			
Perturbation current	A	0.05			
Temperature	°C	785			
OCV recorded	V	0.934	0.938	0.937	0.938
OCV theoretical	V	0.939	0.939	0.939	0.939
Difference	mV	5	1	2	1

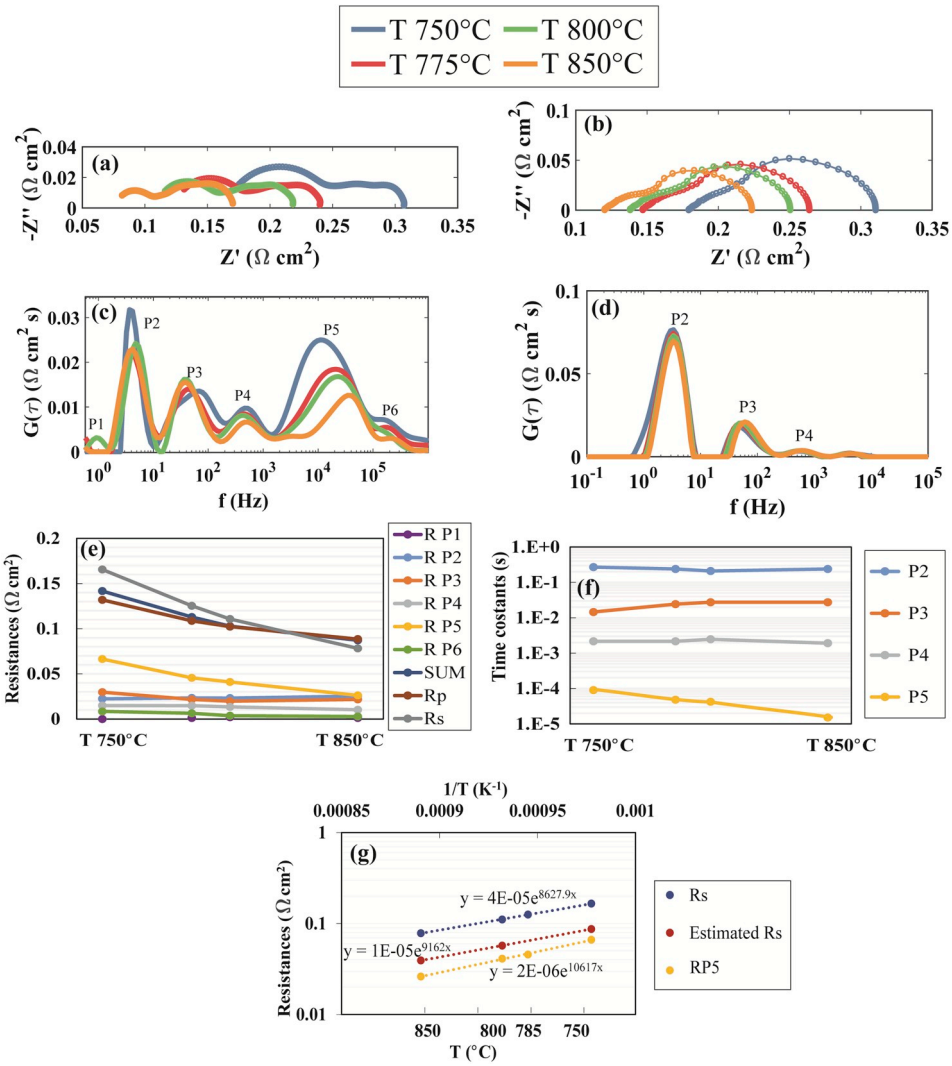

Fig. 1. EIS dependence on temperature. (left) Experimental (right) Numerical model. simulation. (a) and (b) Nyquist plot. (c) and (d) corresponding DRT. (e) Evolution of the ohmic (Rs), polarization (Rp), and individual resistances. (f) Evolution of the individual time constants. (g) Characteristic dependence of ohmic and charge transfer resistances on the operating temperature, linear trend equations have been used for activation energy calculation.

from 66.36 to 26.16 mΩ cm^2 and for P6 from 8.4 to 2.6 mΩ cm^2 (Fig. 1 (e)). The thermal activation of P5 is expected as it is related to distributed charge transfer in the fuel electrode. P4 also exhibits a decreasing trend (resistance reduction of 45%). However, P2 and P3 do not vary consistently.

Estimates of the activation energies of the elementary processes can be measured from temperature dependent experiments. The resistances of thermally activated processes (P5 and the ohmic resistance Rs) are plotted against the inverse of the temperature (Arrhenius plot in Fig. 1 (g)). The calculated activated energy, based on the numerical value of the exponential law reported in Fig. 1(g), for Rs is 72 kJ mol^{-1} (0.75 eV). A rough estimation has been carried out to assess the expected activation energy for this contribution, by considering the conductivities of the different layers composing the studied single cell. The ionic conductivity of YSZ [18] and GDC [19], the total conductivity of the Ni:YSZ support [20], the electrical conductivity of LSCF [21] and the oxygen electrode contact layer [22] have been considered along with the ionic conductivity of the composite LSCF:GDC. The total ohmic resistance generated by the cell has been computed as series connection among the different layers, considering their thickness and a correction factor for the porous structure according to Eq. (10):

$$R \cdot A = \frac{1}{\sigma} L \frac{(1-\varepsilon)}{\tau^2} \tag{10}$$

where A is the area, σ is the conductivity expressed in S cm^{-1}, L is the thickness, ε is the porosity, and τ is the tortuosity.

The ionic conductivity of LSCF:GDC has been computed according to Eq. (11) [23] and multiplied by an estimated penetration depth (in the order of few micrometers) [24]:

$$\sigma_{ion} = \frac{4F^2 D_v \delta}{RTV_m} \tag{11}$$

Here, F is the Faraday constant, D_v the vacancy diffusion coefficient, δ is the oxygen non stoichiometry, R is the Gas constant, T is the temperature and V_m is the molar volume of the composite electrode. Even by increasing of 20% the value of the ohmic resistance due to the possible formation of an insulating $SrZrO_3$ phase, the value of the estimated resistances is almost one third lower than the measured ohmic resistances. It suggests that other contributions should be considered, such as current constriction at contact points between dense and porous layers, the formation of solid solutions at the electrolyte/compatibility layer interface and current collection contact resistance. The main

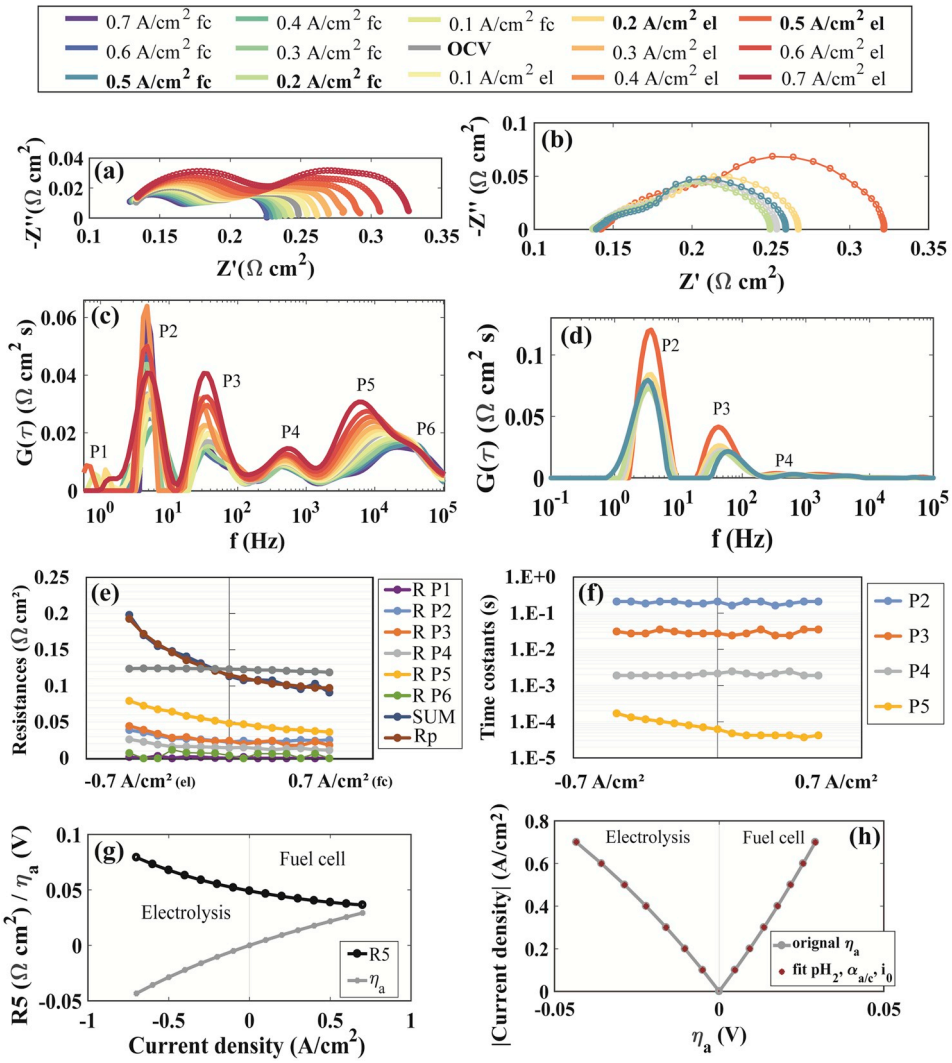

Fig. 2. EIS dependence on current density. (left) Experimental (right) Numerical model. simulation. (a) and (b) Nyquist plot. (c) and (d) corresponding DRT. (e) Evolution of the ohmic (Rs), polarization (Rp), and individual resistances. (f) Evolution of the individual time constants. (g) Anodic activation overpotential obtained from the integration of the charge transfer resistance (RP5) (h) Fitting of the activation overpotential by Butler-Volmer formulation.

contributions to the estimated values are the electrolyte and the GDC layer followed by the ion transport in the active oxygen electrode layer. The calculated activation energy resulting from the estimated ohmic resistance is in line with the measured value and equal to 0.79 eV. The activation energy of the charge transfer resistance is equal to 0.93 eV. The activation energy reported in literature for this process lies between 0.75 and 1.6 eV [8,25–27].

The reduction of the ohmic resistance (Rs) is captured in the simulated spectra (Fig. 1(b)). From the deconvoluted model spectra (Fig. 1 (d)) some other details are visible: increasing the temperature causes a decrease of the conversion peak (P2) and a slight increase of the resistances associated to the fuel and oxygen electrode side transport peaks (P3 and P4) which are also moved to slightly higher frequencies.

The comparison of the model and the recorded spectra (Fig. 1(c) and (d)) highlight few notable discrepancies. Firstly, P4 varies, even though it not is expected to be thermally activated. A possible explanation is that the high frequency peak (P5) is not totally deconvoluted and it causes an increase in peak P4, which should remain constant. P2 and P3 vary inconsistently due to experimental noise in the mid/low frequencies range that affect the deconvolution.

Fig. 1(e) confirms the trend of the calculated resistances: (i) the ohmic resistance (Rs) variation is predominant; (ii) the polarization resistance calculated from the Nyquist plot (Rp) and by summing the individual resistances (SUM) agree well; (iii) P5 and P6 and Rs are the thermally activated processes (iv) the decrease in P4 with increasing temperature may be due to an imperfect deconvolution of peak P5 since the numerical model suggests that the diffusion peak should not change. The time constant trend in Fig. 1(f) reveals a shift of the peak P5 to higher frequencies.

4.2. Current density

In this section the spectrum evolution due to variations of the current from 0.7 A cm^{-2} (FC mode) to −0.7 A cm^{-2} (electrolysis mode) is reported, considering a binary mixture of H_2/H_2O 50-50% at the fuel side at 800 °C (Table 3). The OCV value, reported in Table 3 is in line with those measured in the temperature variation experiment.

Moving from electrolysis to fuel cell mode causes a decrease of the polarization losses but does as expected not influence the ohmic resistance (Fig. 2(a)). The DRT plot (Fig. 2(c)), allow better identification of the elementary processes variation. The peak showing the most significant change by varying the current is P5, the characteristic frequency of which moves from 20 kHz to 5 kHz, as the current density is varied from 0.7 A cm^{-2} (cell polarized in fuel cell mode) to −0.7 A cm^{-2} (cell polarized in electrolysis mode). During the current change between the two extreme values, the trend of the resistance associated to P5 follows

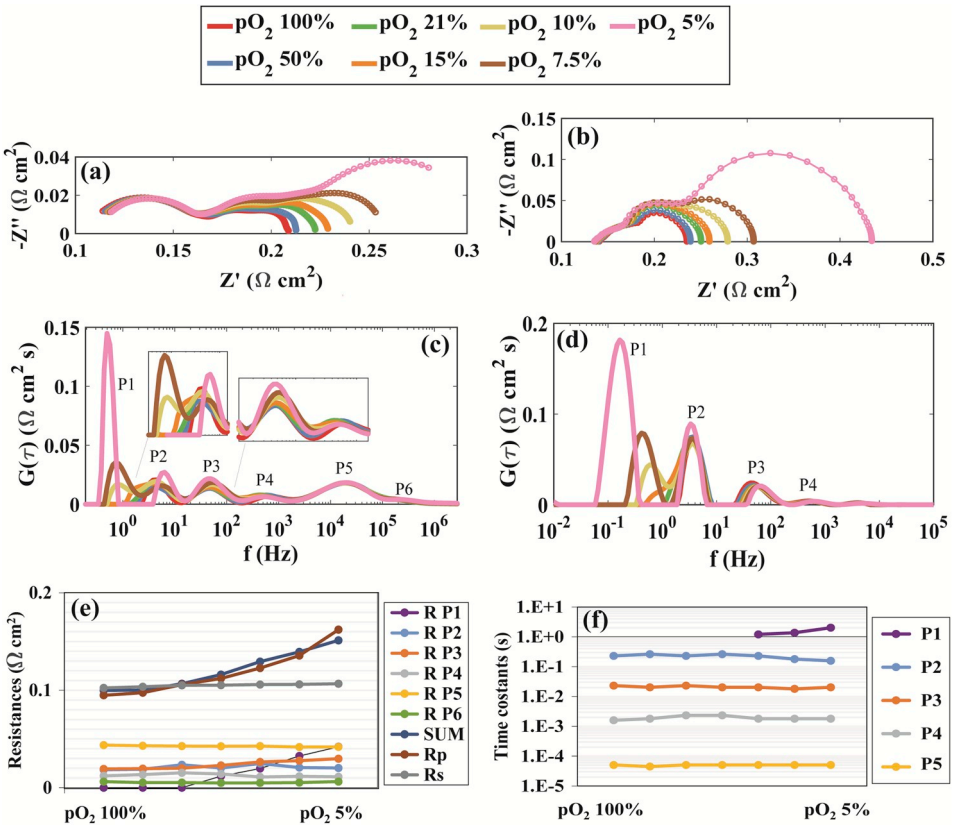

Fig. 3. EIS dependence on oxygen partial pressure. (left) Experimental (right) Numerical model simulation. (a) and (b) Nyquist plot. (c) and (d) corresponding DRT. (e) Evolution of the ohmic (Rs), polarization (Rp), and individual resistances. (f) Evolution of the individual time constants.

an exponential decay law (yellow curve in Fig. 2(e)). Although the resistance decreases as the current density in fuel cell mode increases, the resistance increases as the current density in electrolysis mode increases. Moreover, the increase recorded in electrolysis mode is higher than the decrease registered in fuel cell mode. Peak P5 is attributed to charge transfer at the fuel electrode. An evidence of this attribution is the relation between the evolution of the resistance of this process and the Butler-Volmer expression. In fact, the fuel electrode overpotential can be retrieved by integration of the fitting equation describing the evolution of this resistance [4], this last being computed as the area below the peak P5 in the DRT (Fig. 2(c) and (e)). Knowing from the experiment $\eta_{act,a}$ and i, and from the DGM computation $x_{H_2}^{TPB}$ and $x_{H_2O}^{TPB}$ the remaining parameters for fitting in Eq. (2) [8] are the exchange current density (i_0^*) and the anodic and cathodic symmetry factors (α_a and α_c).

The estimated values of these three parameters are respectively 0.925 A cm^{-2}, 1.23 and 0.75 (red dots in Fig. 2(h)). The different symmetry factors may to be related to the differences in the rate limiting mechanisms occurring in the two polarization modes [8]. However, P5 obeying Butler-Volmer kinetics does not explain why the resistance increases for electrolysis polarization but decreases in fuel cell mode. Purely geometrical calculations were performed and suggest that if the Butler-Volmer expression is symmetric, the resistance should decrease upon increasing the magnitude of current in either way. However, if different symmetry factors are imposed, the resistance decreases in one direction and increases in the other. In particular, the asymmetry in this case indicates that the charge transfer is facilitated in the oxidation direction. Besides P5, the processes most sensitive to current are P2 and P3 followed by P4. The ohmic resistance and P6 are almost constant while P1 is not always observed. The peak P2, and thus its associated resistance (Fig. 2(c) and (e)), attributed to gas conversion, shows as expected a decrease and a subsequent increase, upon passing from electrolysis to FC mode. The resistance drops from 39 mΩ cm^2 at −0.7 A cm^{-2} to 22 mΩ cm^2 at OCV and subsequently increases again to 25 mΩ cm^2 at 0.7 A cm^{-2}. The parabolic trend of the conversion peak is justified by the fuel electrode concentration overpotential equation expression (Eq. (12)), that forecasts minimum losses when 50-50% H_2/H_2O mixture is used.

$$\eta_{conc,a} = \frac{RT}{2F} \ln\left[\frac{p_{H_2}^{GC} p_{H_2O}^{TPB}}{p_{H_2}^{TPB} p_{H_2O}^{GC}}\right] \tag{12}$$

Whenever the cell is under polarization at a non-negligible FU (in this case 15% at highest current density), deviations from this value are recorded, causing an increase in resistance. The characteristic frequency of this process does not change by changing the current, but it is scattered around 4 Hz. For this reason, the associated capacitance value evolves in a near-reverse manner with respect to the resistance (Fig. 2 (e)). The anode diffusion and cathode transport peaks (P3 and P4) present a monotonically decreasing trend when changing the current from −0.7 to 0.7 A cm^{-2} (Fig. 2(d)). The resistance variation is higher in electrolysis compared with fuel cell regime. The characteristic frequencies for P3 and P4 are respectively spread around 50 Hz and 500 Hz. In Fig. 2(b) and (d), the simulated Nyquist and DRT plot of the simulated spectra are reported. Only five current values are simulated, corresponding to the bold characters in the top legend of Fig. 2. The numerical model captures well the trend of P2, P3 and P4. Peak P3, is mostly affected by fuel electrode diffusion. As seen in Fig. 2(e), the resistance related to this process in electrolysis mode is nearly twice the resistance at the same current density in fuel cell mode.

4.3. Oxygen partial pressure

The influence of variation in oxygen partial pressure on EI spectra has been analyzed considering a 50-50% fuel mixture of H_2/H_2O at 800 °C under a current bias of 0.3 A cm^{-2} (in FC mode). The full set of

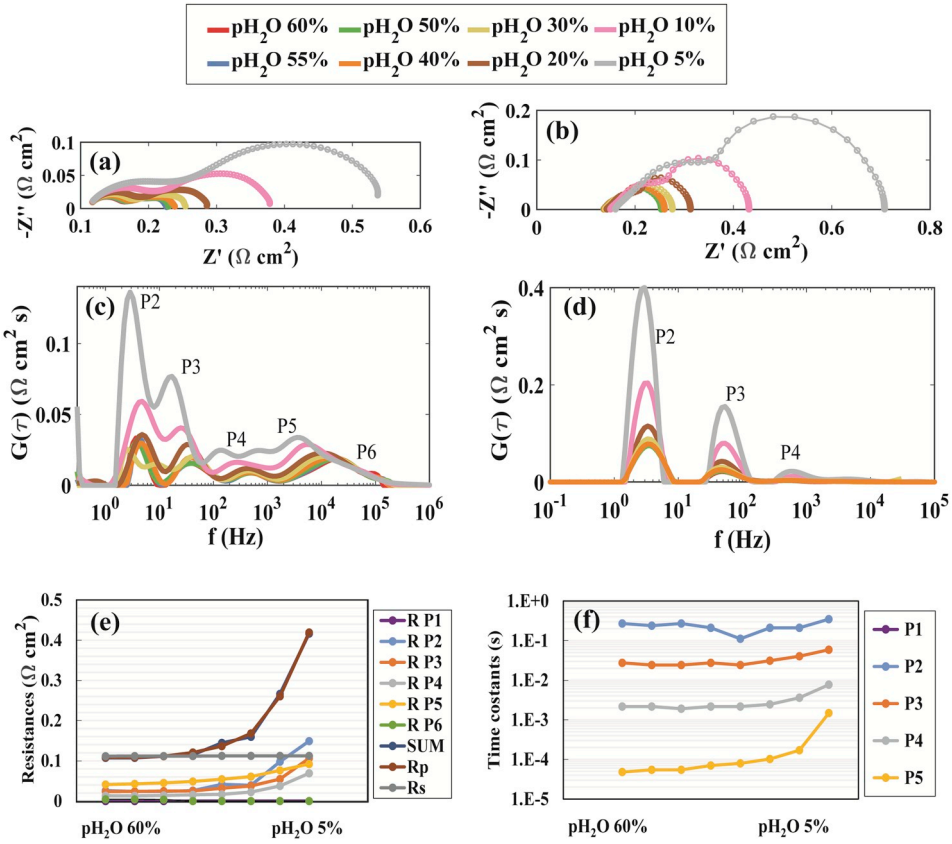

Fig. 4. EIS dependence on steam partial pressure on fuel side. (left) Experimental (right) Numerical model simulation. (a) and (b) Nyquist plot. (c) and (d) corresponding DRT. (e) Evolution of the ohmic (Rs), polarization (Rp), and individual resistances. (f) Evolution of the individual time constants.

operating conditions is reported in Table 4. Decreasing the partial pressure of oxygen from 100 to 5% provokes an increase of the polarization resistance but does not influence the ohmic resistance, as visible in Fig. 3(a). Fig. 3(c), reports the DRT of the spectra together with the zoom of peak P2, P3 and P4 to visually inspects the trends of the different peaks. This graph highlights that the peak that varies the most is P1, followed by P3. P1 peak does generally not show a clear evolution trend and it is not always apparent, principally because: (i) under normal operating conditions, this loss is negligible in magnitude; (ii) at low frequencies the spectrum is prone to be affected by noise, which can mask or modify this peak. In Fig. 3(c), peak P1 becomes clearly visible when pO_2<21%. Only a shoulder on peak P2 is visible at $pO_2 = 15\%$ that increases and moves towards lower frequency when the partial pressure decreases to 5%. From Fig. 3(e) the value of the P1 resistance that increases from 0 to 47 mΩ cm^2 can be read. The P1 characteristic frequency decreases and consequently the increase in characteristic time is shown in Fig. 3(f). This peak has been attributed to oxygen electrode diffusion [4,28] or an adsorption/desorption limiting mechanism at very low oxygen partial pressure [29,30].

The conversion peak P2 does not show a particular variation in its resistance and maintains a value around 20 mΩ cm^2 but it is slightly shifted towards higher frequency (Fig. 3(e)). Its unchanged resistance could suggest that peak P1 is also related to oxygen conversion. If peak P1 was not related to conversion, the share of the conversion losses linked to the oxygen partial pressure variation should add up to the fuel conversion resistance and increase the resistance of peak P2, which is not observed experimentally. From the DRT plot of the experimental (Fig. 3(c)) and simulated (Fig. 3(d)) spectra a mild dependence of peak P3 on the oxygen partial pressure can be noticed. The peak resistance increases upon decreasing the oxygen partial pressure from 19 to 30 mΩ cm^2. Even if the model predicts a variation of peak P3, the predicted trend is not consistent with the experimental one, which warranties further investigations. Peak P4 is barely sensitive to the oxygen partial pressure and its resistance as well as its characteristic frequency are respectively centered around a mean value of 10 mΩ cm^2 and 500 Hz, as predicted by the model. Lastly, looking at peaks P5 and P6, the complete absence of variation upon oxygen partial pressure variation confirms the full attribution of peak P5 to fuel electrode charge transfer and raises new questions on the possible attribution of P6 to solid-solid oxygen electrode transfer processes [2,29] or to electronic current losses between the oxygen electrode and the current collector [31].

It is worth mentioning that under conditions of practical relevance for stack operation low partial pressure of oxygen are not expected because of the high air excess.

4.4. Steam partial pressure on fuel side

This section is focused on the influence of the steam partial pressure on the impedance spectra of a SOC. The experiments have been carried out at 800 °C at OCV with air fed to the oxygen electrode and a variable composition of H_2/H_2O on the fuel side. In particular, eight different steam partial pressures have been investigated, ranging from 5 to 60% of steam content in the hydrogen flow (Table 5). Fig. 4 reports the experimental ((a) and (c)) and simulated ((b) and (d)) impedance spectra. Also in this case the polarization resistance is strongly influenced by the change of the fuel electrode gas composition whereas the ohmic resistance remains unaffected.

The deconvoluted spectra plot (Fig. 4(c)) shows the peaks evolution with the steam partial pressure, while their relative resistances are reported in Fig. 4(e). The conversion peak P2 is strongly influenced by the steam partial pressure content. This peak decreases as the steam partial pressure increases, reaches a minimum when the steam content is 50% and subsequently increases again. The same is predicted by the

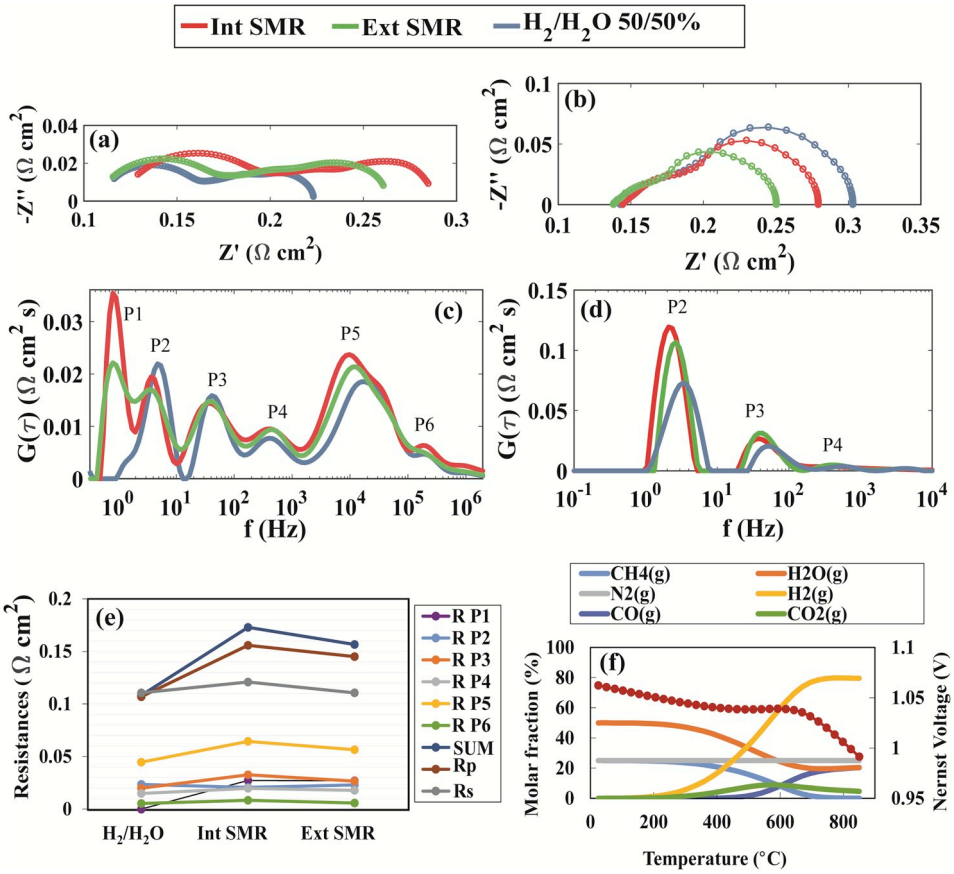

Fig. 5. EIS dependence on fuel composition. (left) Experimental (right) Numerical model. simulation. (a) and (b) Nyquist plot. (c) and (d) corresponding DRT. (e) Evolution of the ohmic (Rs), polarization (Rp), and individual resistances. (f) Equilibrium composition calculation and expected Nernst voltage.

numerical EIS model for which the symmetrical H_2/H_2O partial pressure conditions, 40/60% and 60/40% are perfectly coincident as presented in Fig. 4(d). As discussed before, P3 and P4 are slightly influenced by oxygen partial pressure variation, and Fig. 4(c) shows that these peaks are greatly influenced by the steam partial pressure variation. Therefore, fuel electrode diffusion and oxygen electrode transport occur in the middle frequency range and so cannot be totally deconvoluted. The resistance associated to peak P3 under the most limiting conditions, 5% pO_2 and 5% pH_2O, is 30 mΩ cm^2 and 106 mΩ cm^2, respectively. Therefore, gas-phase transport in the fuel electrode is more limiting than cathode transport under normal operating conditions. This is expected given the fuel and oxygen electrode thickness difference. Peak P4, however, seems influenced only by the steam partial pressure. Both fuel electrode diffusion and cathode reaction/transport impedance in the DRT plot show secondary peaks of small intensity located at higher frequency than their main peaks. Peak P4 is in fact in the same frequency range as the secondary peak of the P3 diffusion process. Also the charge transfer peak (P5) increases when the steam partial pressure is lowered. The resistance associated to this process (Fig. 4(e)) increases from 41 to 92 mΩ cm^2 when decreasing from 60 to 5% H_2O in H_2. Furthermore, considering the characteristic time constants (Fig. 4(f)) of the different processes it follows that lowering the steam content in the fuel feed causes the peaks to shift towards smaller frequencies. Such a shift is not foreseen by the model (Fig. 4(d)). The peculiarity of Fig. 4(e) is the possibility to identify the main limiting phenomena in the neighborhood of the OCV: (i) at low steam partial pressure (<5%) the losses related as conversion > fuel electrode diffusion > charge transfer, (ii) at partial pressure around 10% they relate as conversion > charge transfer > fuel diffusion, (iii) for steam partial pressure higher than 20% finally the loss order is charge transfer > conversion > diffusion.

4.5. Fuel composition

The effect of the variations in fuels is here analyzed. Similar operating conditions as for the previous experiments are imposed: the operating temperature is 800 °C and the polarization current is 0.3 A cm^{-2}. The purpose of the test was to assess how the operation with methane changes the distribution of the losses in a SOFC. For this reason, three compositions are compared as reported in Table 6. The H_2/H_2O 50-50% gas composition is compared to:

- INTERNAL REFORMING: CH_4 25%-H_2O 50% diluted with 25% of N_2. This mixture, corresponding to S/C (steam to carbon) ratio equal to 2, is directly fed to the cell without pre-reforming. Since 1 mol of CH_4 provides 4 mol of H_2 due to the WGS and SMR reactions, the total flow rate has been adjusted to 25 NmL min^{-1} of CH_4, which is equivalent to 100 NmL min^{-1} of H_2. Moreover, to avoid transport limitation in the setup, dilution with 25% of N_2 was added.
- EXTERNAL REFORMING: H_2 53.3%-H_2O 13.3%-CO 13.2%-CO_2 3.5%-CH_4 0%-N_2 16.7%. This gas mixture represents the equilibrium composition for CH_4 25%-H_2O 50%-N_2 25% at 800 °C, calculated with HSC software [32] (Fig. 5(f)). Thus, it corresponds to a fully externally reformed mixture equilibrated at 800 °C.

Table 6 lists the OCV values for the three compositions. Although there is a good match between the recorded and the calculated value for hydrogen, the two other mixtures present a difference of about 100 mV. The theoretical value has been calculated considering the computed oxygen concentration in the equilibrium mixture [32] and using the Nernst expression:

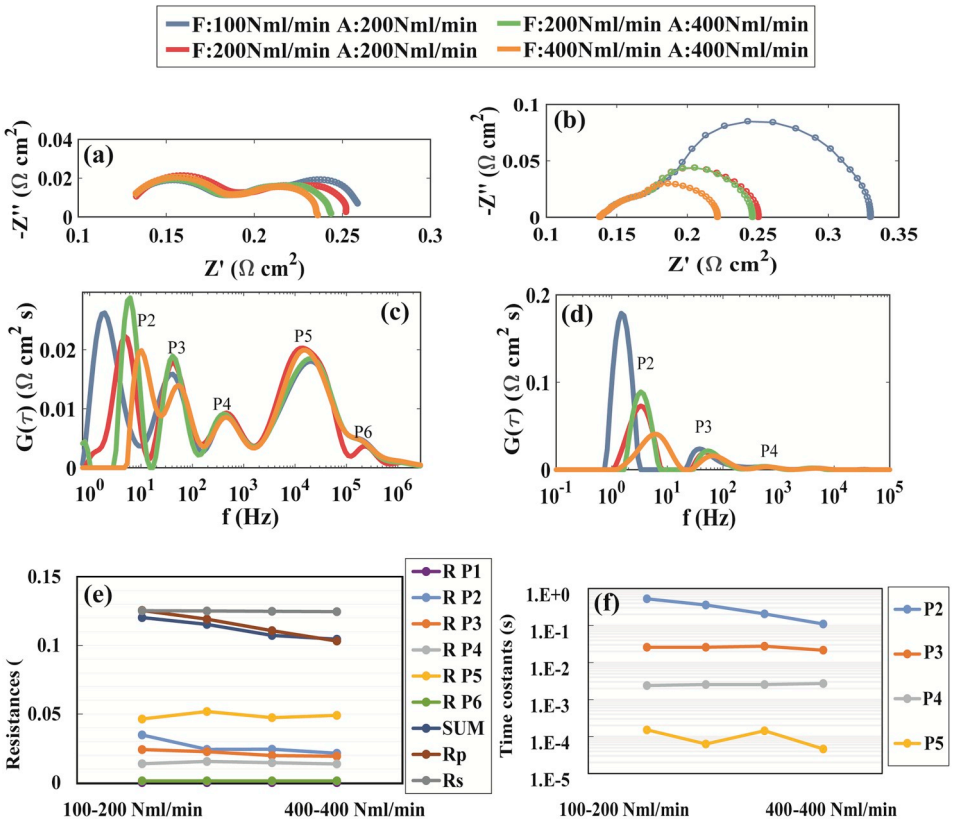

Fig. 6. EIS dependence on total flows. (right) Experimental (left) Numerical model. simulation. (a) and (b) Nyquist plot. (c) and (d) corresponding DRT. (e) Evolution of the ohmic (Rs), polarization (Rp), and individual resistances. (f) Evolution of the individual time constants.

$$E = \frac{RT}{4F}\ln\left[\frac{p_{O_2}^{red}}{p_{O_2}^{ox}}\right] \tag{13}$$

In addition to the deviation from the Nernst potential, the OCV values measured under internal and external reforming conditions, present a difference of 7 mV. Looking at the Nyquist plot in Fig. 5(a), the same ohmic resistance of 0.11 Ω cm^2 is observed for the H_2/H_2O mixture and the externally reformed mixture. Meanwhile, an ohmic resistance of 0.13 Ω cm^2, is recorded under internal steam reforming. In Fig. 5(c) the evolution of the elementary processes is better visualized. First of all, the main difference between hydrogen and methane operation is at low frequency (<1 Hz), where a new peak is visible. The peak is indicated as PR since it has generally been attributed to the reforming reaction occurring at the fuel electrode [33]. According to Kromp [33], this peak is associated to the diffusion of CO/CO_2 produced in the fuel electrode under reforming conditions. Despite the fact that only a partial experimental analysis was carried out during this set of measurements, the same dependency at low frequency upon different CO/CO_2 mixtures has been reported for the same cell and test bench than that observed in the present analysis [34]. In the present case, PR is larger under internal than external reforming operation. The conversion peak (P2), which has smaller amplitude than in the hydrogen/steam case, presents the same behavior. No major differences are recorded for peak P3, whereas an increase of peak P4 is visible while switching from the hydrogen mixture to the external reformed one. The effect of the fuel compositions on the charge transfer peak (P5) is similar to what observed for peak P4. Multiple hypotheses can be formulated to explain the variation of peaks with respect to the fuel composition:

- The difference in PR and P2 between the internally and externally reformed mixture can arise from the fuel composition itself. In particular, it is likely that internal reforming in the cell did not reach equilibrium. Thus, the composition would correspond to higher CO_2 content with respect to the equilibrium composition considered in the externally reformed mixture.
- The introduction of carbon compounds in the fuel tends to increase the peak P4 due to the presence of larger molecules. A thermal effect can be the cause of the larger charge transfer peak observed in the internal reforming case. The combined effect of the SMR and reverse Water Gas Shift (rWGS) reaction is endothermic, which lowers the cell temperature. As a consequence, the charge transfer peak is increased (as observed in the temperature variation paragraph) compared to the external reforming case. Moreover, it is possible that different rate limiting steps may come into play when the composition is changed causing the observed modifications.

The numerical model has been used to simulate impedance spectra in the hope of improving the understanding of the nature of PR. Unfortunately, the presence of the low frequency peak (<1 Hz) was not captured (Fig. 5(d)), which thereby brought no further information.

The actual model considers fast kinetics for the WGS reaction that equilibrates in the anode support. The SMR reaction, as explained in the EIS model section, is modeled according to the empirical Achenbach kinetics [35]. Refined kinetics modelling is likely needed to better predict the experimental observation. Moreover, the attribution of the peak PR to diffusion [33] rather than to conversion needs further dedicated investigations. Simulations of EI spectra with the transient diffusion DGM in CO/CO_2 atmosphere indicates an increase of the diffusion resistance but only a slight variation of the time constant that was shifted from around 50 to 20 Hz.

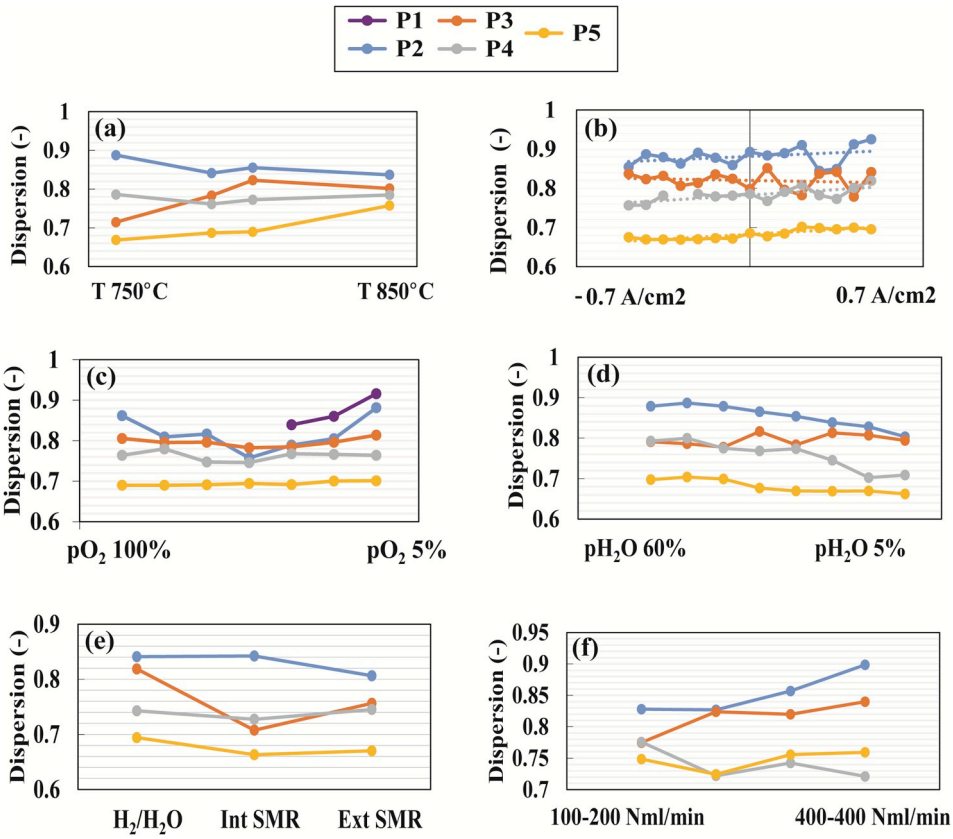

Fig. 7. ZARC dispersion parameter variation upon operating condition variation: (a). temperature, (b) current, (c) oxygen partial pressure, (d) steam partial pressure, (e) fuel composition, (f) total flow.

4.6. Total flow

In this section, the influence of the fuel and air flow rates on the electrochemical spectra is investigated. Four different flows were examined at 0.3 A cm^{-2}, 785 °C, under air-H_2/H_2O 50/50% gas composition. The first measurement is performed with a fuel flow rate of 100 NmL min^{-1} and doubled air flow. In the second, equal flow rates of 200 NmL min^{-1} were fed to both electrodes. The third and fourth measurements are performed with doubled flows with respect to the first two measurements. Table 7 lists the operating conditions along with the measured and expected OCV. Such a comparison points out that increasing the flow rate reduces the difference between the theoretical and experimental OCV. Only 1 mV difference is recorded for the second and fourth measurements, obtained at the same fuel and air flows. Theoretically, for an H_2/H_2O 50/50% gas composition, conversion losses should be negligible. The Nyquist plot in Fig. 6(a) highlights an increase of the polarization resistance but no changes in the ohmic resistance. From the DRT plot in Fig. 6(c), the trend of the different peaks is examined. The main variation is recorded on peak P2. Theory [36,37] informs that the conversion resistance and the flow rate are inversely proportional, therefore an increased total flow reduces the conversion losses. The analytical expression [37] also indicates that the capacity of the conversion impedance decreases when the flow rate increases. Therefore, the model simulations (Fig. 6(b) and (d)) predict the experimentally observed trends. The fuel diffusion peak (P3) shifts from 40 to 60 Hz between the first and the last measurement (respectively the blue and orange curves in Fig. 6(c) and (d)) is particularly well captured. No modifications of peak P4 are observed and neither predicted. As expected, the fuel flow rate contributes more than the air flow rate to the observed modifications, since it affects the species concentrations. A small modification of the high frequency region, corresponding to the charge transfer peak P5, is visible on the DRT plot (Fig. 6(c)). This is due to a different fuel utilization as well as to variations of in gas compositions among the four spectra. Specifically, the lower charge transfer peak is registered when the fuel flow is half the air flow. For these two conditions, the difference in OCV is higher than the cases in which the air and fuel flow are the same.

The main observations are summarized in the resistance and capacitance trends plotted in Fig. 6(e) and (f): (i) increasing the flow decreases both the conversion resistance and time constant, (ii) the total flow rate influences the diffusion peak, the resistance of which slightly decreases while the time constant remains stable, (iii) an imperfect seal modifies the local partial pressures, which in turn affects the charge transfer resistance. This effect can be mitigated when the same flow rate is imposed at the anode and cathode, which lower the pressure difference between the two gas compartments.

5. Consideration on DRT plots

5.1. CPE dispersion parameters

In the previous section, the magnitude of the resistances and capacitances associated to the elementary processes for the examined operating conditions have been reported. In this section an analysis on the dispersion parameter that results from the peaks fitting to ZARC elements is discussed. In fact, for each peak in the DRT plot the dispersion α can be extracted, besides the resistance (area under each peak) and the time constant (peak positions). In Fig. 7 the dispersion values for the four main peaks (P2, P3, P4, and P5) is plotted for the six operating parameters previously analyzed. The dispersion of the peak P2 is on average 0.85. This value decreases with decreasing steam partial pressure and current. Moreover, it presents a parabolic variation trend

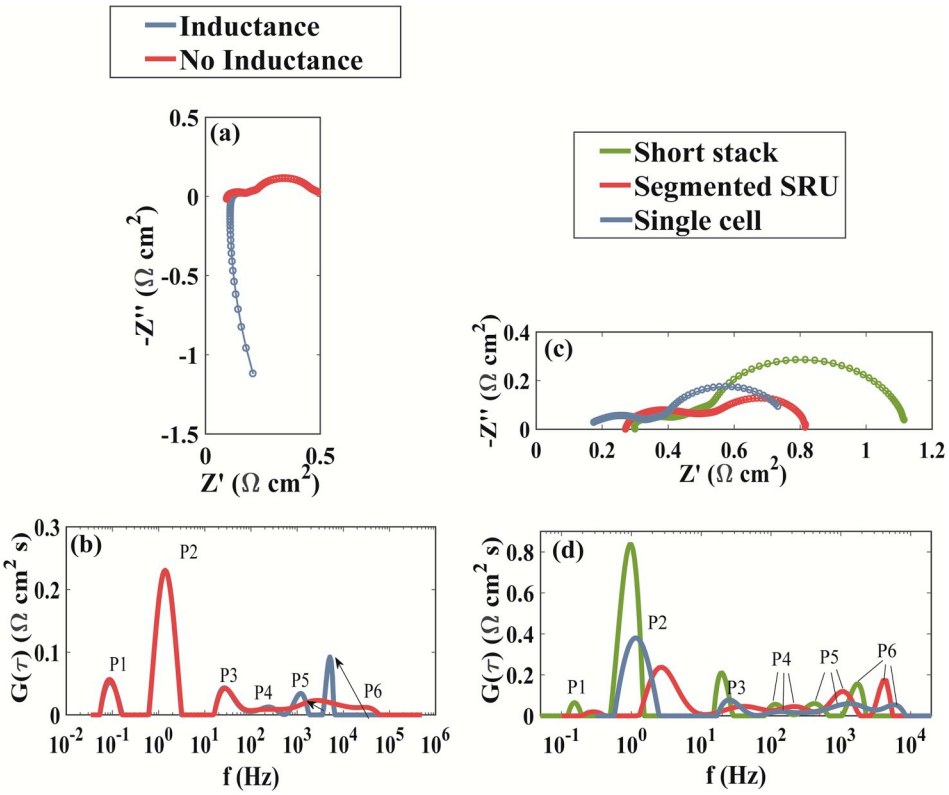

Fig. 8. Left: effect of inductance on DRT. (a) Nyquist Plot. (b) DRT of the two spectra. Right: comparison of EIS obtained at different scale. (c) Nyquist Plot. (d) DRT of the three spectra.

upon oxygen partial pressure variation from 100 to 5% concentration. The dispersion of peak P3, the average value of which is scattered around 0.8, increases by increasing the fuel flow rate from 100 to 400 NmL min^{-1}. As reported in Refs. [4,38] fuel diffusion can be modeled by a generalized finite length Warburg (G-FLW) element, the estimated dispersion parameter of this peak corresponds to a n_w factor equal to 0.45. n_w equal to 0.5 indicates a perfect one-dimensional diffusion. The α value of peak P4 decreases by decreasing both the current and the steam partial pressure and its average value is 0.77. The charge transfer peak (P5) generally presents the lowest dispersion average value with respect to the other peaks, equal to 0.72. The value increases by increasing the temperature and decreases by lowering steam partial pressure and current density.

5.2. Effect of the inductance

Beside operating conditions, frequency range and inductance can strongly influence the impedance spectrum and consequently its deconvolution. These effects are clarified hereafter by comparing spectra measured with different instrument configurations (twisted and untwisted wires) and at different SOC geometries and scales (single cell, segmented SRU and short stack (SS)). The presence of inductance in the recorded spectrum affects the DRT and thus has to be corrected or included in the impedance model to obtain meaningful DRT results. Here, a comparison of an experimental EI spectrum with and without inductance is presented. The two measurements were performed on the same cell by twisting the wires from the cell to outside the oven (different from that used for the sensitivity analysis). The only difference between the two situations (Fig. 8) lies in the wiring between the measurement equipment and the test bench: low inductance cables (twisted) are used for the free inductance spectrum, a four-cable (untwisted) configuration is used for the spectrum that presents the inductance. Both spectra are recorded from 500 kHz to 50 mHz. The Nyquist plot in Fig. 8(a) shows the difference in ohmic resistance between the two measurements due to the presence of the inductance. In Fig. 8(b), the DRT plot of the spectra reported in Fig. 8(a) is presented considering the deconvolution obtained by Tikhonov regularization.

Both spectra present six peaks that perfectly coincide at low frequency (<1 kHz) but differ in the high frequency region. In particular, peak P5 shifts from 4 to 1 kHz and peak P6 from 40 to 5 kHz. Changes in the amplitudes of the peaks at high frequency are linked to the reallocation of the polarization resistance in more a restricted frequency range, since the total area under the DRT spectrum must be equal in the two cases (same polarization resistance). Along with the frequencies shift, the measured contributions of the elementary processes to the total polarization losses change. In the inductance-free spectrum, they are respectively: P1 10%, P2 57.5%, P3 10%, P4 3%, P5 17%, P6 2.5%. The peak shares for the case presenting the inductance are: P1 10%, P2 57.5%, P3 10%, P4 4%, P5 10%, P6 9%. Therefore, the presence of the inductance leads to underestimation of the charge transfer resistance. Since the stack test bench does not allow the twisting of wires, the presence of inductance effects at high frequency are unavoidable. Therefore, while analyzing the DRT deconvoluted spectra this effect should be accounted for.

5.3. Comparisons of different geometries

Different cell sizes and geometries are compared in this section: a single cell, a short stack (SS), and one segment of a segmented SRU (on the flow inlet side) [3]. The spectra obtained with the three different geometries are all recorded with the same gas mixture, 60/40% dry H_2/N_2 as fuel and air as oxidant, at a temperature of 750 °C. A current density of 0.1 A cm^{-2} is used for the single cell and short stack while 0.15 A cm^{-2} is used for the segmented SRU. The short stack and the

Table 8
DRT peaks attribution and their variation upon operating conditions variation.

	P1	P2	P3	P4	P5	P6
	Conversion diffusion at low pO_2 transport in reforming mixture	Gas conversion	Fuel electrode diffusion/oxygen electrode reaction + solid state diffusion	Secondary peaks (fuel and oxygen electrode transport)	Fuel elctrode charge transfer	High f. Peak (?)
Parameters	pO_2	$F_{tot} > pH_2 > i > pO_2 > T$	$pH_2O > i > F_{tot} > pO_2 > T$	$pH_2O > T > pO_2$	$T > i > pH_2O$	T
Temperature (T) ↑	–	–	–	↓	↘	↓
Current density (i)↑	–	↘↗	↙	↓	↘	–
Oxygen partial pressure (pO_2) ↑	↘	–	↓	–	–	–
Steam partial pressure (pH_2O) ↑	–	↓	↓	↘	↘	–
Total flow rate (F_{tot}) ↑	–	↘	–	–	–	–
Frequency	**< 1Hz**	**1–10 Hz**	**10–100 Hz**	**0.1–0.5 kHz**	**0.5-up to 100 kHz**[a]	**5- up to 200 kHz**[a]
Single cell no L	0.1	4	50	0.5	20 (2)	200 (6)

() values obtained in a different experiments with respect to the sensitivity one.
↑-increase, ↓-decrease, ↘-decrease and shift towards right.
↙-decrease and shift towards left, ↘↗-decrease and increase while shifting towards right.
[a] Characteristic frequency influenced by inductance and frequency range.

segmented cell are fed with the same fuel and air flow rates, respectively 6 and 67 NmL min^{-1} cm^{-2}, whereas the single cell is fed with 8 and 16 NmL min^{-1} cm^{-2}.

Beside the operating conditions, other differences exist among these three scales:

- the flow distribution is radial for the single cell and longitudinal co-flow for the SS and segmented SRU;
- the cell geometry and active area is circular for single cell (12.56 cm^2) and rectangular for the SS (80 cm^2);
- different frequency ranges: 50 mHz to 40 kHz for the single cell, 100 mHz to 25 kHz for the segmented cell and 100 mHz to 10 kHz for the short stack;
- cell connection and wiring: single cell twisted wires, and SS/segmented SRU co-axial current roads and individual untwisted voltage wires for each of the six elements.

For the short stack and the segmented SRU, inductance correction is performed to assess the value of the ohmic resistance, equal to 0.17 and 0.3 Ω cm^2 for the single cell and SS/segmented SRU, respectively, as can be seen in Fig. 8(c). From the DRT analysis reported in Fig. 8(d), a consistent number of peaks at each scale has been found, despite some differences in the position of the characteristic times at high frequency. These can be explained by the presence of the inductance in the short stack and segmented SRU measurement spectra when compared to the single cell spectrum. Moreover, the difference between the short stack and the segmented repeat unit is attributed to the truncated frequency range of the former (necessary to exclude inductive behavior from 10 to 100 kHz). The conversion peak (P2) variation between the short stack and single cell is due to the different flow rates used. The difference between these two and the segmented SRU is due to a slightly different current density and probably to the influence of the neighboring segments. Nevertheless, the present comparison confirms for the first time directly that different cell geometries and test benches arrangements have a consistent number of peaks under the same operating conditions. Due to different assemblies, the inductance shape and the frequency range can vary, causing deviations especially at high frequency.

6. Conclusion

An analysis of sensitivity of the locations and amplitudes of DRT peaks with regard to operating conditions has been presented. The attribution of the peaks to physical processes was assisted by numerical modelling, especially in the mid-frequency region where oxygen and fuel electrode mechanisms overlap.

(i) Variation of the temperature have shown that the ohmic resistance, the charge transfer peak (P5) and the highest frequency peak (P6) are thermally activated processes.
(ii) The current density influences the spectra over the whole frequency range. The charge transfer peak (P5) is the most sensitive, the trends in the relationship of its associated resistance upon current density variations is in accordance with a modified Butler-Volmer equation. The conversion peak (P2) follows a parabolic trend reflecting variations in the gas composition due to different fuel utilizations. Diffusion losses in the fuel electrode (P3 and P4) are larger in SOEC than SOFC mode suggesting that the electrode microstructure can be further improved.
(iii) Oxygen partial pressure variation mainly affects the resistance of the peak at very low frequency (P1). Oxygen variation influences also peak P3 though to milder extent compared to steam partial pressure.
(iv) Steam partial pressure modifies all the peaks between P2 and P5, especially the conversion peak (P2) and the diffusion peaks (P3 and P4). In the middle frequency range the overlap with the oxygen electrode mechanisms could be clearly shown. Since the diffusion peaks (P3 and P4) are more sensitive to this parameter than oxygen partial pressure, fuel side transport losses dominate those on the oxygen side.
(v) Internal and external steam reforming comparison have confirmed the presence of an additional peak at low frequency (<1 Hz) with respect to hydrogen fuel operation. First model simulations suggest that the peak is not related to CO/CO_2 diffusion, but further investigations are needed. The analysis point that the main difference between internal and external steam reforming is likely induced by distinct temperature gradients.
(vi) Total flow variations indicate that the conversion peak (P2) can be heavily reduced by increasing this parameter. Moreover, the total flow slightly affects the diffusion peaks proving that conversion and diffusion mechanisms are coupled.

The analysis was further extended to the effects of inductance, frequency range and different cell configurations:

(i) The inductance effect at high frequency can be limited by twisting the voltage and current pairs of wires. When twisting is not possible, the inductance effect can be handled by the DRT routine in two ways: (a) by introducing an inductance element in the fitting model of the DRT function (b) by performing a correction [39]. These procedures are exactly equivalent as long as the shape of the inductance is perfectly straight, i.e., it only affects the imaginary part of the spectrum. The presence of the inductance leads to an underestimation of the resistance of the charge transfer peak.

(ii) The frequency range has to be wide enough to include the characteristic time constants of all the phenomena (from mHz to kHz). A smaller frequency range results in a shift of the characteristic frequencies (for the high frequencies peaks) towards lower frequencies and can lead to a smaller number of detectable peaks.

In Table 8 a summary of the results discussed in the previous sections is presented.

Acknowledgements

The research leading to these results has received funding from the Swiss State Secretariat for Education, Research and Innovation SEFRI under contracts 16.0199 and 16.0042 corresponding to the European Union's Horizon 2020 research and innovation programme (Fuel Cells and Hydrogen 2 Joint Undertaking) projects under grant agreement No 735918 (INSIGHT) and 700667 (SOSLEM).

Dr. Antonio Bertei and Dr. Andrè Weber are warmly acknowledged for the precious advices and discussion. Jan Pieter Ouweltjes and Dr. Zacharie Wuillemin from SOLIDpower SA are thanked for the discussion on the experimental results.

List of symbols

Latin letters

A	active area/cm^2 or m^2
a	volume specific internal surface area/m^2 m^{-3}
c	concentration/mol cm^{-3} or mol m^{-3}
c_v	concentration of vacancy/mol cm^{-3} or mol m^{-3}
c_M	mass concentration/kg m^{-3}
D	diffusion coefficient/cm^2 s^{-1} or m^2 s^{-1}
E	Nernst voltage/V
E_0	standard cell voltage/V
F	Faraday's constant/C mol^{-1}
f	frequency/Hz
i	current density/A cm^{-2} or A m^{-2}
i_0	exchange current density/A cm^{-2} or A m^{-2}
i_{ampl}	current perturbation amplitude/A cm^{-2} or A m^{-2}
j	imaginary unit/
L	length/m
M	molecular weight/g mol^{-1}
n	specific molar flow/mol s^{-1} cm^{-2} or mol s^{-1} m^{-2}
p_x	species partial pressure/bar
R	Gas constant/J mol^{-1} K^{-1}
R	area specific resistance/Ω cm^2 or Ω m^2
$\Re$	rate of species production/mol s^{-1} m^{-2}
T	temperature/K or °C
t	time/s
U	cell voltage/V
V_M	molar volume/cm^3 mol^{-1} or m^3 mol^{-1}
v	velocity/m s^{-1}
x	molar fraction/

Greek letters

$\alpha_{c/a}$	charge transfer coefficient/
$\delta_{p/g}$	thickness/cm or m
δ	penetration depth/cm or m
ε	porosity/
η	overvoltage/V
θ	phase shift/rad
ρ	density/kg m^{-3}
τ	tortuosity/

Subscripts/Superscripts

a	anodic
act	activation
c	cathodic
fl	fuel electrode
GC	gas channel
MIEC	mixed ionic electronic conductor
Ohm	ohmic
ox	oxygen electrode or oxidation
pol	polarization
red	reduction
v	vacancy

References

[1] A. Weber, J. Szász, S. Dierickx, C. Endler-schuck, E. Ivers-tiffée, ECS Trans. 68 (2015) 1953.
[2] R.R. Mosbaek, Ph.D. Thesis, Technical University of Denmark, Kongens Lyngby, Denmark, 2014.
[3] Z. Wuillemin, et al., ECS Trans. 57 (2013) 561.
[4] A. Leonide, Ph.D. Thesis, Karlsruhe Institute of Technology, Karlsruhe, Germany, 2010.
[5] M. Kornely, N.H. Menzler, A. Weber, E. Ivers-Tiffee, Fuel Cells 13 (2013) 506.
[6] D. Montinaro, A.R. Contino, A. Dellai, M. Rolland, Int. J. Hydrogen Energy 39 (2014) 21638.
[7] A. Nakajo, P. Tanasini, S. Diethelm, J. Van herle, D. Favrat, J. Electrochem. Soc. 158 (2011) B1102.
[8] D.G. Goodwin, H. Zhu, A.M. Colclasure, R.J. Kee, J. Electrochem. Soc. 156 (2009) B1004.
[9] V. Menon, Q. Fu, V.M. Janardhanan, O. Deutschmann, J. Power Sources 274 (2015) 768.
[10] S.D. Ebbesen, X. Sun, M.B. Mogensen, Faraday Discuss 182 (2015) 393.
[11] H. Zhivomirov, Phase Difference Measurement, Can Be Found under, 2016. https://it.mathworks.com/matlabcentral/fileexchange/48025-phase-difference-measurement-with-matlab-implementation.
[12] H. Madi, et al., J. Power Sources 279 (2015) 460.
[13] D. Klotz, A. Weber, E. Ivers-Tiffée, Electrochim. Acta 227 (2017) 110.
[14] H. Schichlein, A.C. Muller, M. Voigts, A. Krugel, E. Ivers-Tiffé, J. Appl. Electrochem. 32 (2002) 875.
[15] T.H. Wan, M. Saccoccio, C. Chen, F. Ciucci, Electrochim. Acta 184 (2015) 483.
[16] B.A. Boukamp, J. Electrochem. Soc. 142 (1995) 1885.
[17] M. Schönleber, D. Klotz, E. Ivers-Tiffée, Electrochim. Acta 131 (2014) 20.
[18] J.-H. Park, R.N. Blumenthal, J. Electrochem. Soc. 136 (1989) 2867.
[19] C.M. Kleinlogel, L.J. Gauckler, J. Electroceram. 53 (2000) 231.
[20] A. Nakajo, et al., J. Electrochem. Soc. 158 (2011) B1083.
[21] M. Lubini, et al., J. Phys. Chem. C 120 (2016) 64.
[22] M. Sogaard, P.V. Hendriksen, M. Mogensen, F.W. Poulsen, E. Skou, Solid State Ionics 177 (2006) 3285.
[23] J.E. ten Elshof, H.J.M. Bouwmeester, H. Verweij, Solid State Ionics 81 (1995) 97.
[24] S.B. Adler, J.A. Lane, B.C.H. Steele, J. Electrochem. Soc. 143 (1996) 3554.
[25] W.G. Bessler, et al., Phys. Chem. Chem. Phys. 12 (2010) 13888.
[26] J. Mizusaki, et al., Solid State Ionics 70–71 (1994) 52.
[27] A. Utz, Ph.D. Thesis, Karlsruhe Institute of Technology, Karlsruhe, Germany, 2011.
[28] J. Hjelm, M. Sogaard, M. Wandel, M. Menon, M. Mogensen, A. Hagen, ECS Trans. 7 (2007) 1261.
[29] A. Bertei, G. Arcolini, J.P. Ouweltjes, Z. Wuillemin, P. Piccardo, C. Nicolella, Electrochim. Acta 208 (2016) 129.
[30] M. Hubert, et al., Solid State Ionics 294 (2016) 90.
[31] L. Almar, J. Szász, A. Weber, E. Ivers-Tiffée, J. Electrochem. Soc. 164 (2017) F289.

[32] H. Chemistry, Can Be Found under, 2018. http://www.hsc-chemistry.net/.
[33] A. Kromp, Ph.D. Thesis, Karlsruhe Institute of Technology, Karlsruhe, Germany, 2013.
[34] G. Rinaldi, S. Diethelm, J. Van herle, ECS Trans. 68 (2015) 3395.
[35] E. Achenbach, E. Riensche, J. Power Sources 52 (1994) 283.
[36] T. Jacobsen, P.V. Hendriksen, S. Koch, Electrochim. Acta 53 (2008) 7500.
[37] S. Primdahl, M. Mogensen, J. Electrochem. Soc. 145 (1998) 2431.
[38] J.R. Macdonald, Impedance Spectroscopy: Emphasizing Solid Materials and Systems, John Wiley & sons, 1987, p. 87.
[39] B. Liu, T. Matsui, H. Muroyama, K. Tomida, T. Kabata, K. Eguchi, J. Chem. Inf. Model. 53 (2011) 637.